Hiding Extra-Framework Cations in Zeolites L and Y by Internal Ion Exchange and its Effect on CO_2 Adsorption

Magdalena M. Lozinska,[a] David N. Miller,[a] Stefano Brandani[b] and Paul A. Wright[a,*]

[a] *EaStCHEM School of Chemistry, University of St. Andrews, Purdie Building, North Haugh, St Andrews, Fife, KY16 9ST, Scotland*

[b] *Institute for Materials and Processes, University of Edinburgh, King's Buildings, Mayfield Rd, Edinburgh, EH9 3JL, Scotland*

[†] *For Electronic Supplementary Information see DOI:*****************. For crystallographic files see CCDC 1950850-1950855, 1970061 and 1970062. The research data supporting this publication can be accessed at DOI: The research data underpinning this publication can be accessed at* https://doi.org/10.17630/1fff8eca-c51d-4c6e-a8a9-0ec83939479c

Abstract

The fully La-exchanged form of the large pore zeolite L, $La_{3.0}Al_{9.0}Si_{27.0}O_{72}$, has been prepared by repeated aqueous ion exchange and internal cation exchange resulting from calcination to give a low silica zeolite (Si/Al = 3) with all cations hidden from available porosity. This results from the migration of La^{3+} from sites in the large 12-membered ring (12R) channel (exchangeable via aqueous solution) to 'closed' sites in the structure. The mechanism for this internal cation exchange, which has been elucidated by Rietveld analysis of powder X-ray diffraction data, comprises sequential La^{3+} migration, first to *ste* cages between cancrinite (*can*) cages in the framework and then into the *can* cages. In each case K^+ cations must first leave the closed cages, in the first case through 8Rs, in the second via puckered 6Rs. The first migration step is achieved by 573 K, the second by 1073 K. Decrease of the K^+ occupation in accessible main channel sites of zeolites $K_{9.0}$-, $K_{5.7}La_{1.1}$-, $K_{2.7}La_{2.1}$- and $La_{3.0}$-L strongly

changes the shape of the CO_2 adsorption isotherms, as the strength of interaction decreases. The Henry Law constant for $K_{9.0}$-L zeolite is 36.60(2) mol (kg bar)$^{-1}$, whereas for $La_{3.0}$-L it is 1.80(3) mol (kg bar)$^{-1}$, if an initial uptake of 0.1 mmol g^{-1} is neglected. The isosteric heat of adsorption is correspondingly strongly reduced. A CO_2 isotherm shape similar to that observed for La-L is also shown by a fully-exchanged La-Y, $La_{18.7}Al_{56.0}Si_{136.0}O_{384}$, prepared from Na-Y by repeated aqueous and internal ion exchange. In this case the internal exchange requires the egress of Na^+ cations from sodalite cages via planar 6R windows and so is possible at lower temperatures (<673 K). The ability to modify CO_2 isotherm shape in low silica zeolites by hiding cations in inaccessible cages can be of interest to tailor pressure swing adsorbents for a range of CO_2-containing gas streams.

Introduction

The large pore zeolite L has been investigated extensively for applications in catalysis, particularly in the aromatisation and (de)hydrogenation of hydrocarbons,[1,2] and the encapsulation of luminescent dyes[3] and lanthanide complexes[4] for optical sensing applications. These properties result from interactions of guest molecules within the large pore channels present in the zeolite. The aluminosilicate framework structure of zeolite L (topology type LTL) is built from columns of alternating *d6r* (double 6Rs, consisting of 6 tetrahedral Si or Al atoms and 6 O atoms*)* and *can* (cancrinite) cages, linked via *ste* cages (Figure 1a and b). Together, these give rise to a hexagonal array of large channels bounded at their narrowest by 12Rs (with a free diameter of 7.1 Å) and opening out to form large 'supercages' with a free diameter of 12 Å. Charge-balancing extra-framework cations have been reported to occupy three different sites in zeolite L (Figure 1c and d). While sites I and II are 'closed' sites within the *can* and *ste* cages, site III is located in 8R sites opening out onto the large channels, where

its cations can coordinate water molecules in the hydrated form. The relatively low Si/Al ratio of ca. 3 that is typical of as-synthesised zeolite K-L is such that in the as-prepared K-form ($K_{9.0}Al_{9.0}Si_{27.0}O_{72}$) most (4 out of 6) of the main channel sites are occupied, and are accessible to guest molecules, and so strongly influence adsorption properties.

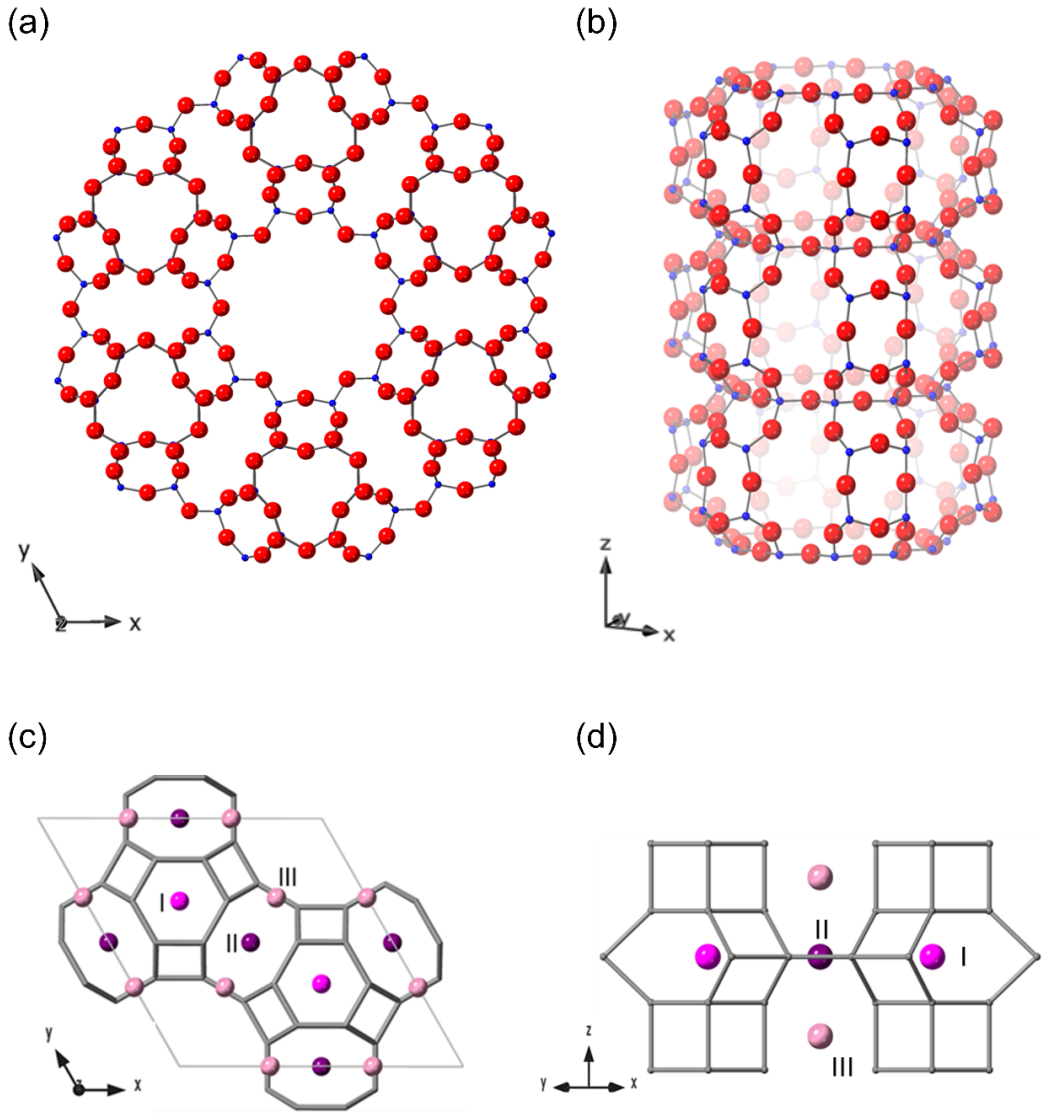

Figure 1. Representation of the framework structure of zeolite L ((a) and (b), O atoms red and Si/Al atoms blue), which is constructed of columns of *can* cages and *d6r* units and contains 12R channels. In dehydrated zeolite $K_{9.0}$-L ((c) and (d)), K^+ cations occupy three sites: the centre of the *can* cage (coordinates (x, 2x, ½), x ≈ 0.3, denoted site I here), midway between two neighbouring *can* cages (coordinates (0, ½, ½), site II) and near the wall of the

12R channel (coordinates (0, y, 0), y ≈ 0.3, site III). Framework O atoms are omitted for clarity and T−T linkages are represented by grey sticks.

Only cations in the large channel sites can readily be exchanged under aqueous conditions, although it has been reported that some non-main-channel cations can be exchanged by ammonium ions.[5] Indirect measurements have shown that it is possible, however, to replace cations in otherwise 'closed' sites I and II via a combination of aqueous ion exchange and calcination at high temperature. This must result from solid-state ion exchange between sites, including the *can* cage sites. Similar effects have been observed in other zeolites, some of which, like zeolite L, contain *can* cages.[6–13] While conventional aqueous ion exchange of zeolites erionite, offretite and cancrinite below 373 K does not reduce the K^+ cation content in the can cages, series of cation exchanges and calcinations at *ca.* 573 K can do this, via a process of internal ion exchange. Close crystallographic study of the structural changes involved in this cation exchange[8] has shown that in erionite, for example, dehydration is followed by K^+ cation diffusion from the *can* cage to the neighboring erionite cage and the counter migration of Ca^{2+} cations into the *can* cage where they occupy sites with higher coordination by O atoms. The migration of Ca^{2+} cations to the *can* cage produces a favourable six-fold coordination with framework O atoms, and changes in the unit cell dimensions as the larger K^+ ion is replaced by Ca^{2+}.[8,9,11] While the *can* cages in these zeolites are connected via distorted 6Rs into large open cages or channels, those in zeolite L are connected via distorted 6Rs to fully-occupied *ste* cage sites, so that a more concerted mechanism of cation migration must be operative in this zeolite.

In principle, the composition of zeolite L should allow for complete removal of extra-framework cations from the main channel by a combination of aqueous and internal ion exchanges with di- or trivalent cations, if their occupation of cage sites is favoured thermodynamically, as expected by consideration of coulombic effects. It should then be

possible to prepare a family of L zeolites with tunable wide channel cation contents, all the way to an end-member material with large one-dimensional channels lined with O atoms, but with all extra-framework cations hidden away, and these materials should have characteristic behavior as adsorbents.

Typically, alkali metal cation forms of zeolites with Si/Al = 3 exhibit steep Type I adsorption isotherms at room temperature for polar molecules such as CO_2 because of strong cation-CO_2 interactions. These materials give effective purification of gas streams but, as a consequence of their isotherm shape, have reduced working capacities in pressure swing adsorption applications if low desorption pressures are not achieved. Therefore, it was of interest to investigate the effect on the CO_2 adsorption isotherm of reducing the effect of the extra-framework cations. It also gives information on the extent of the internal cation exchange via an independently-measured physical property.

The sequential aqueous and high temperature internal cation exchange of La^{3+} into zeolite K-L has been measured via Rietveld refinement analysis of X-ray powder diffraction data. The difference in scattering of La^{3+} compared to K^+, as well as its smaller size, enables cation site occupancies to be determined, and enables constraints on the mechanism to be established. Exhaustive repetition produces a La-only zeolite L for the first time. The CO_2 adsorption isotherms and Henry law constants of a series of progressively La-exchanged L zeolites have been measured and related to the cation site occupancies. Furthermore, the isosteric heats of adsorption of CO_2 for the K- and La-end members have been compared.

Recognising that a prolonged process is required to prepare La-L with all La^{3+} cations hidden, a fully La-exchanged zeolite Y was also prepared, in order to compare its CO_2 adsorption behaviour. La^{3+} ion exchange and migration is well known in zeolite Y, where the La^{3+} cations

migrate from supercages into sodalite (*sod*) cages upon dehydration at temperatures as low as 373 K.[14] In industry, rare-earth (RE) ion-exchanged zeolite Y that possesses acidity and enhanced stability is typically prepared from commercial Na-Y zeolite using a double-exchange double-calcination method.[15] Here, adsorption of CO_2 on a fully La-exchanged zeolite Y prepared via a similar route is compared with that on the La-L materials to establish common features of these 'hidden-cation' zeolite adsorbents.

Experimental

Zeolite L (LTL), $K_{9.0}Al_{9.0}Si_{27.0}O_{72}$ ($K_{9.0}$-L) was synthesised using a modification of a previously reported procedure (S1, Electronic Supplementary Information (SI))[16] and converted to different cation compositions using a combination of aqueous ion exchange and internal solid-state ion exchange. $K_{9.0}$-L (1.0 g) was repeatedly ion exchanged with 0.5 M lanthanum or calcium nitrate solution at 333 K for 2-4 h and calcined at 1073 K in flowing oxygen gas for 10 h until desired compositions were achieved (with ca. 1, 2 and 3 La per unit cell, for K,La-L). Details are given in the SI, but as an example, for $La_{1.1}K_{5.7}$-L, ten aqueous ion exchanges were necessary, and then the sample was heated at 1073 K for internal ion exchange. For the fully-exchanged $La_{3.0}$-L, $K_{9.0}$-L was exchanged 100× and calcined 10× at 1073 K.

For comparison, commercially-obtained Na-Y ($Na_{56.0}Al_{56.0}Si_{136.0}O_{384}$, $Na_{56.0}$-Y), was ion exchanged with 0.5 M lanthanum nitrate solution at 333 K for 6 h. Fully-exchanged $La_{18.7}$-Y was ion exchanged 10× and heated twice at 673 K.

Scanning electron microscopy with energy dispersive X-ray spectroscopy (SEM-EDX) was used to determine compositions. The EDX analysis on all samples was performed in a JEOL JSM 5600 SEM, with an Oxford INCA Energy 200 EDX analyser. For $K_{9.0}$-L, the only peaks

from extra-framework cations were at X-ray energies from K, whereas substitution of K with La resulted in the additional appearance of peaks at La L-line X-ray energies. The ratio of the intensities of the K X-ray peaks to the La X-ray peaks decreased with increasing lanthanum content until only the lanthanum peaks were present, indicating complete substitution of potassium by lanthanum (SI, S2).

The crystallinity of as-prepared, cation-exchanged and dehydrated samples was confirmed by laboratory powder X-ray diffraction (PXRD) using a Stoe STAD I/P diffractometer with Cu $K_{\alpha 1}$ X-radiation (1.54056 Å). In order to determine the structure of dehydrated zeolites, the powders were loaded into 0.7 mm quartz glass capillaries and dehydrated at 623 K for 12 h at 5 x 10^{-5} mbar on a glass vacuum line before flame sealing. The PXRD patterns of the dehydrated samples were obtained from these capillaries.

The sample of $La_{3.0}$-L for STEM analysis was crushed in a mortar and pestle, dispersed in ethanol and deposited on a holey carbon film supported on a copper grid. The holey carbon film had been sputter-coated with gold to assist in alignment of the aberration corrector of the STEM. K-LTL samples was prepared by a conventional focused ion beam (FIB) techniques using a FEI Scios FIBSEM. A small quantity of $K_{9.0}$-L particles was first deposited on a Si substrate, a suitable particle was identified by SEM and a thin protective platinum layer (~250 nm) was applied by electron beam deposition, followed by a thicker the ion deposited layer (1.5 μm). The FIB was then used to thin the sample to electron transparency. High angle annular dark field (HAADF)-STEM measurements were carried out using a spherical aberration corrected (Cs-corrected) FEI Titan Themis 200 transmission electron microscope equipped with a high brightness Schottky X-FEG emitter and operated at 200 kV with a convergence angle of 20 mrad. The column was fitted with a Cs DCOR aberration corrector, which was aligned using a standard gold sample prior to every experiment. The multi-slice

method was used to produce simulated HAADF images using the QSTEM software developed by Christoph Koch.[17]

Thermogravimetric analysis (TGA) was performed on a NETZSCH TG1000 M in a dry air flow with a heating rate of 5 K min^{-1} to 1073 K. CO_2 adsorption isotherms were measured gravimetrically on a Hiden Intelligent Gravimetric Analyzer (IGA) at 298 K. All samples were activated at 573 K for 6 h prior to measurements. To quantify the interaction of CO_2 with sorbents, Henry Law constants (K_H) were estimated from the intercepts of plots of $\ln(n/p)$ vs. n, where n is the uptake, as shown in the Supporting Information. Some of the isotherms showed a small initial uptake (ca. 0.1 mmol g^{-1}) at very low pressures due to uptake on strong binding sites. To avoid the strong effect of this on K_H, this uptake was subtracted before deriving K_H from plots of $\ln(n/p)$ vs. n.

Additionally, CO_2 adsorption isotherms were measured from 0-2 bar at 278, 288 and 298 K on the IGA. The isosteric heats of adsorption were determined using the Clausius-Clapeyron equation at uptakes from 0.75 to 1.5 mmol g^{-1}. The isotherms were first fitted by virial equations using Desmos software[18] and subsequently pressures giving specific uptakes were obtained from these fits.

Crystallography

The structures were determined by Rietveld refinement against the PXRD data, using the GSAS suite of programs.[19] For as-prepared zeolite $K_{9.0}$-L, starting framework models were adapted from the literature with the unit cell modified to that derived from the diffraction pattern.[5,20] Starting cation positions were estimated from literature models and the framework atomic positions were initially refined with geometric restraints on T-O (T = Si or Al; 1.64 ± 0.02 Å) and O-O (2.65 ± 0.02 Å) distances to maintain regular tetrahedral coordination[5,20] and

these restraints were gradually removed throughout the refinement process. Final extra-framework cation sites and occupancies were determined by the refinement of starting positions and by using difference Fourier methods to look for additional sites. Three cation sites were found which agreed with positions reported in the literature.[5,20] A similar procedure was followed for $La_{3.0}$-L. For fully exchanged $La_{3.0}$-L all occupancies were refined as La^{3+} cations since no potassium was detected by EDX analysis. The refined cation occupancy is in agreement with the EDX analysis. Unit cell constants and cation site occupancies for $K_{9.0}$-L and $La_{3.0}$-L, and refined T-O framework distances and T-O-T angles, are given in Tables 1 and 2 respectively, and Rietveld plots are given in Figure 2.

Table 1. Unit cell parameters, site occupancies in dehydrated zeolites $K_{9.0}$-L and the La-exchanged series.

Zeolite	Unit cell parameters (Å)	Site I		Site II		Site III	
		Frac. Occup.	Atoms per unit cell	Frac. Occup.	Atoms per unit cell	Frac. Occup.	Atoms per unit cell
$K_{9.0}$-L	18.4388(2) 7.4877(1)	1.02(1) (K)	2.05(1) (K)	1.01(1) (K)	3.03(1) (K)	0.641(2) (K)	3.85(1) (K)
$K_{5.7}La_{1.1}$-L (before calcination)	18.2837(2) 7.5023(1)	1.03(1) (K)	2.06(1) (K)	0.734(7) (K) 0.264 (La)	2.02(1) (K) 0.792 (La)	0.245(4) (K) 0.0462 (La)	1.47(1) (K) 0.277 (La)
$K_{5.7}La_{1.1}$-L (after calcination)	18.3958(2) 7.4257(1)	0.676(4) (K) 0.324(4) (La)	1.35(1) (K) 0.648(1) (La)	0.537(6) (K) 0.160 (La)	1.61(1) (K) 0.480 (La)	0.465(4) (K)	2.79(1) (K)
$K_{2.7}La_{2.1}$-L (before calcination)	18.3017(2) 7.4319(1)	0.584(5) (K) 0.372(5) (La)	1.17(1) (K) 0.744(5) (La)	0.451(2) (La)	1.35(1) (La)	0.253(4) (K)	1.52(1) (K)
$K_{2.7}La_{2.1}$-L (after calcination)	18.3889(3) 7.3759(1)	0.365(5) (K) 0.635(5) (La)	0.730(5) (K) 1.27(1) (La)	0.269(2) (La)	0.807(2) (La)	0.321(5) (K)	1.93(1) (K)
$La_{3.0}$-L	18.1425(6) 7.3646(2)	0.851(5) (La)	1.70(1) (La)	0.332(3) (La)	0.996(2) (La)	0.0432(2) (La)	0.259(2) (La)

Table 2. T-O bond lengths (Å), T-O-T angles (°) and distances of K^+ and La^{3+} cations to framework oxygen atoms (Å).

	$K_{9.0}$-L	**$K_{5.7}La_{1.1}$-L (before calcination)**	**$K_{5.7}La_{1.1}$-L (after calcination)**	**$K_{2.7}La_{2.1}$-L (before calcination)**	**$K_{2.7}La_{2.1}$-L (after calcination)**	**$La_{3.0}$-L**
T1-O1	1.636(3)	1.627(5)	1.612(5)	1.609(6)	1.576(6)	1.604(11)
T1-O2	1.623(3)	1.606(4)	1.606(4)	1.601(4)	1.591(5)	1.619(6)
T1-O4 (x2)	1.647(3)	1.662(4)	1.631(5)	1.637(5)	1.626(6)	1.564(8)
Mean T1-O	1.6383	1.6293	1.6200	1.6210	1.6047	1.5878
T2-O3	1.641(3)	1.655(4)	1.645(4)	1.636(5)	1.669(5)	1.610(7)
T2-O4	1.625(4)	1.610(6)	1.638(5)	1.608(6)	1.615(6)	1.696(8)
T2-O5	1.647(2)	1.636(3)	1.644(3)	1.637(3)	1.641(4)	1.675(6)
T2-O6	1.623(2)	1.619(2)	1.621(2)	1.619(3)	1.617(3)	1.613(4)
Mean T2-O	1.6338	1.6299	1.6369	1.6248	1.6354	1.6485
T1-O1-T1	131.2(6)	130.0(8)	130.0(8)	129.3(9)	136.0(10)	120.7(2)
T1-O2-T1	150.2(5)	153.5(8)	155.1(8)	156.4(9)	154.6(10)	153.4(1)
T2-O3-T2	139.1(4)	138.5(5)	136.8(5)	139.3(6)	135.4(6)	136.4(9)
T1-O4-T2	145.2(3)	143.8(4)	145.8(4)	146.6(4)	148.8(5)	147.1(6)
T2-O5-T2	143.9(4)	142.3(5)	144.0(6)	143.2(6)	143.7(7)	133.0(10)
T2-O6-T2	154.5(4)	152.9(5)	158.3(6)	158.3(7)	161.9(7)	159.8(11)
K1/La1-O3 (x6) (site I)	2.883(5) (K)	2.869(6) (K)	2.823(7)(K,La)	2.853(8) (K,La)	2.780(8) (K,La)	2.772(12) (La)
K1/La1-O5 (x6) (site I)	3.387(5) (K)	3.425(7) (K)	3.385(7) (K)	3.384(8) (K)	3.343(9) (K)	-
K2/La2-O4 (x8) (site II)	3.282(3) (K)	3.205(4) (K)	3.273(4) (K)	-	-	-
K2/La2-O5 (x4) (site II)	2.948(5) (K)	2.893(7)(K,La)	2.913(7)(K,La)	2.890(8) (La)	2.899(8) (La)	2.690(12) (La)
K3/La3-O4 (x4) (site III)	3.040(4) (K)	3.02(4) (K) 3.01(5) (La)	3.035(6) (K)	3.012(7) (K)	3.047(7) (K)	2.927(8) (La)
K3/La3-O6 (x2) (site III)	2.825(5) (K)	2.75(8) (K) 2.72(11) (La)	2.883(9) (K)	2.79(1) (K)	2.917(12) (K)	2.62(2) (La)

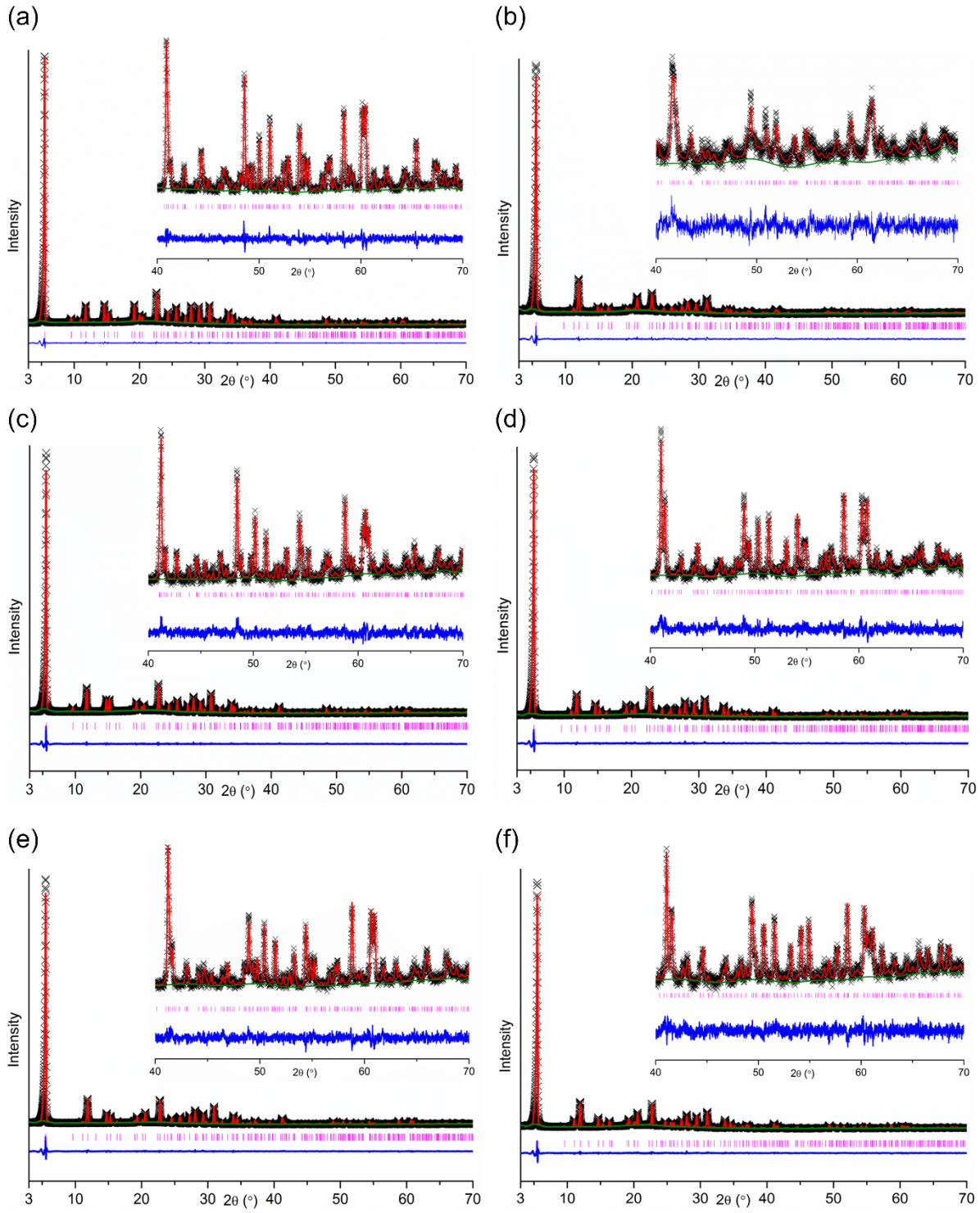

Figure 2. Rietveld plots of PXRD profiles (λ = 1.54056 Å, T = 298 K) of dehydrated (a) $K_{9.0}$-L, (b) $La_{3.0}$-L, $K_{5.7}La_{1.1}$-L (c) before and (d) after calcination, $K_{2.7}La_{2.1}$-L (e) before and (f) after calcination (Observed – black, calculated – red, difference – blue, phase – pink and background – green).

For mixed cation La,K-zeolites L, the La^{3+} and K^+ cations can in principle occupy all three sites, and so the assignment of electron density can be ambiguous. Therefore, a strategy was adopted to determine the fractional occupancy of each cation site by a combination of Rietveld refinement and compositional analysis. Initial refinements assuming all scattering was from K^+ gave fractional occupancies for sites I and II in excess of one in some cases, indicating the heavier La^{3+} cations had migrated into those sites, behaviour that had previously been observed for $La_{3.0}$-L, where there was no ambiguity. For $K_{5.7}La_{1.1}$-L before its calcination, this was observed for site II, while site I remained fully occupied by K. The fractional occupancies of K and La in site II was constrained to sum to one, and allowed to refine. (An initial estimate of the fractional occupancy of La, x_{La}, is given by $x_{La} * 2.87 + (1 - x_{La}) = x_{ref,K}$, where $x_{ref,K}$ is the site occupancy when refined as potassium and 2.87 is the ratio of X-ray scattering factors of La and K for Cu K_α radiation.) The K and La left over after the contents of sites I and II were accounted for, as determined by comparison with the composition measured by EDX, were then attributed to site III and refined in a single position. This process was repeated until convergence.

For $K_{5.7}La_{1.1}$-L after calcination at 1073 K, and $K_{2.7}La_{2.1}$-L before and after its calcination, site I shows an occupancy greater than one when refined as K, so the process of constrained refinement of x_K and x_{La} was adopted, where $x_K + x_{La} = 1$. The additional La measured by EDX was attributed to another site, in this case II, because from the $La_{3.0}$-L structure it was seen that La^{3+} prefers this site over the main channel site. Rietveld plots of the samples $K_{5.7}La_{1.1}$-L and $K_{2.7}La_{2.1}$-L before and after calcination are given in Figure 2 and cation site occupancies and framework geometry are given in Tables 1 and 2, although some ambiguity in the cation occupancy remains due to the assumptions made.

For Ca,K-L zeolites, all extra-framework electron density was attributed to K, due to the very similar X-ray scattering factors for Ca^{2+} and K^{+} cations, and only a (K,Ca) cation occupancy at each site was determined. The unit cell compositions for these samples obtained from EDX analysis were as follows: $K_{6.2}Ca_{1.4}Al_{9.0}Si_{27.0}O_{72}$ ($K_{6.2}Ca_{1.4}$-L) and $Ca_{3.8}K_{1.4}Al_{9.0}Si_{27.0}O_{72}$ ($Ca_{3.8}K_{1.4}$-L). Details are given in the Supplementary Information. CCDC 1950850 to 1950855 contain the supplementary crystallographic data for LTL and can be obtained free of charge from The Cambridge Crystallographic Data Centre.

For Na- and La-Y refinements, a starting model for the Na-Y framework and cation positions (unit cell composition $Na_{56.0}Al_{56.0}Si_{136.0}O_{384}$) was taken from the literature, and structural details and Rietveld plots for the refinements are given in the SI, S3 and S4. CCDC 1970061 and 1970062 contain the supplementary crystallographic data for FAU.

Results and Discussion

A series of La-containing L zeolites was prepared by the repeated aqueous/internal ion exchange procedure. The temperature for internal ion exchange was established via an initial set of experiments in which a partly La-exchanged zeolite L ($La_{0.9}K_{7.1}$-L) was heated at temperatures from 523 K to 1073 K and the structure response monitored using PXRD. Zeolite K-L has previously been found to possess very high thermal stability and remains well-crystalline up to 1087 K.[21] The most obvious changes in relative peak intensities and positions were observed at a temperature of 1073 K. This temperature was therefore chosen as the standard calcination temperature required to achieve internal cation exchange in La-exchanged zeolite L (SI, S5). This temperature is much higher than required for internal ion exchange processes in other zeolites (*ca*. 573 K for erionite, Y, etc.).[8,22]

In this way, zeolite L materials with La contents of 1.1, 2.1 and 3.0 per unit cell were prepared sequentially, and the diffraction pattern of each was measured before and after calcination at 1073 K, following dehydration at 573 K at 10^{-5} mbar for 12 hours. From TGA it was observed that while K-L is fully dehydrated by 500 K, La-containing samples showed a higher temperature weight loss at *ca*. 530 K, extending above 650 K (SI, S6). Prolonged dehydration under vacuum at 573 K is therefore expected to remove all physisorbed water.

PXRD patterns of the zeolites $K_{5.7}La_{1.1}$-L, $K_{2.7}La_{2.1}$-L and $La_{3.0}$-L, each measured in dehydrated form before and after calcination, are shown in Figure 3. The zeolite retains crystallinity, with a minor broadening of peaks only in $La_{3.0}$-L. Rietveld refinement, as described in the Crystallography section, gives unit cell dimensions, framework positions, and cation site occupancies, where cations are located in sites I, II and III (Table 1 and SI, S4). There was no evidence of cations being present within the double 6-membered ring, *d6r,* a fourth extra framework site reported for hydrated zeolite L.[23]

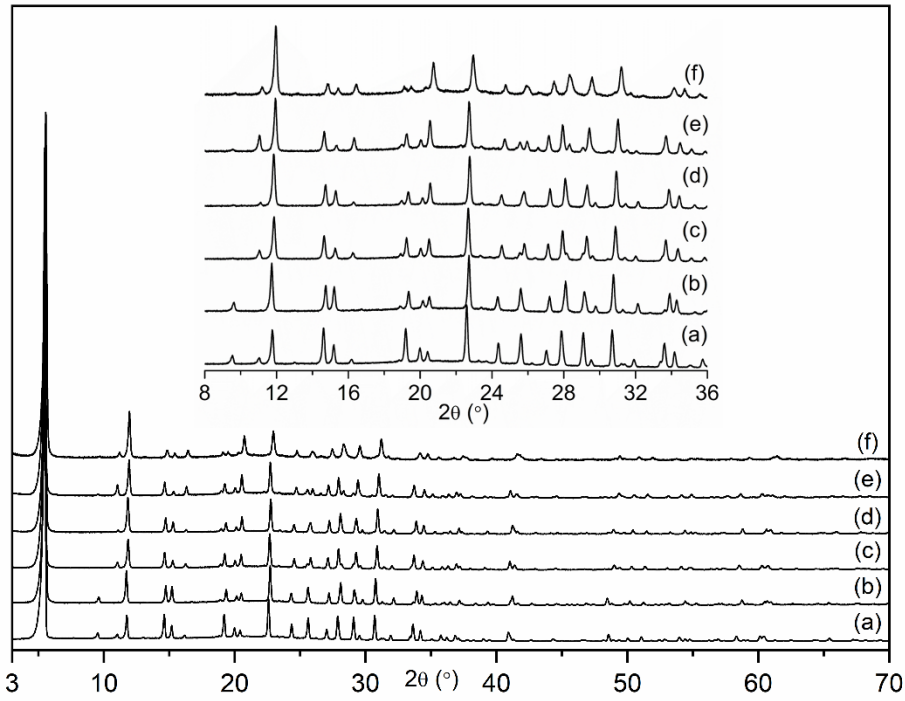

Figure 3. PXRD patterns of dehydrated (a) $K_{9.0}$-L, (b) and (c) $K_{5.7}La_{1.1}$-L before and after calcination, (d) and (e) $K_{2.7}La_{2.1}$-L before and after calcination, and (f) $La_{3.0}$-L. Insert: magnified PXRD from 8° to 36° 2Θ.

Initially, $K_{9.0}$-L possesses fully occupied 'closed' sites I and II, with 4 cations in main channel site III. Extended aqueous ion exchange only gives a La content of 1.1 per unit cell, suggesting that only the main channel sites exchange. Upon dehydration at 573 K, ca. 0.8 of these La cations move to site II, leaving 0.3 behind. This movement must be accompanied by stripping coordinated water molecules from the highly charged cations as they move to a sterically crowded site. Since dehydration results in a low coordination for La^{3+} cations in site III, this favours migration into site II. Whereas in site III each cation is coordinated to 6 O atoms at *ca*. 3 Å or less, as well as coordinated water, in site II each cation is coordinated to 12 O atoms, at 3.3 Å or less (and 4 as opposed to 2 at a distance of *ca*. 2.5 Å). The higher charge of La^{3+} is therefore electrostatically favoured in site II. The La^{3+} cation migration at 573 K must first require a site II to become vacant, which requires a large K^+ cation to move from that site to a vacant site III, allowing La^{3+} to diffuse from its position in site III. This K^+ migration must take place through a buckled 8R of the *ste* cage (Figure 4).

Notably, no La^{3+} is able to migrate to site I at 573 K, even though it is present in the adjacent site II, and subsequent experiments show that its occupation of site I is highly favoured. However, upon calcination at 1073 K, a majority of the 1.1 La^{3+} cations migrate from site II to site I (*ca*. 0.65 La^{3+} cations per unit cell) leaving site III occupied only by K^+ cations (*ca*. 2.8 cations per unit cell). This ion exchange must involve the movement of a K^+ cation in site I through a puckered 6R of the *can* cage (Figure 4) into a site II previously made vacant as described above. A La^{3+} cation in an adjacent site II can then enter site I, where it becomes closely coordinated by 6 O atoms at *ca*. 2.8 Å. The increase in the number of first nearest neighbor O atoms from 4 to 6 appears to be the dominating electrostatic driving force.

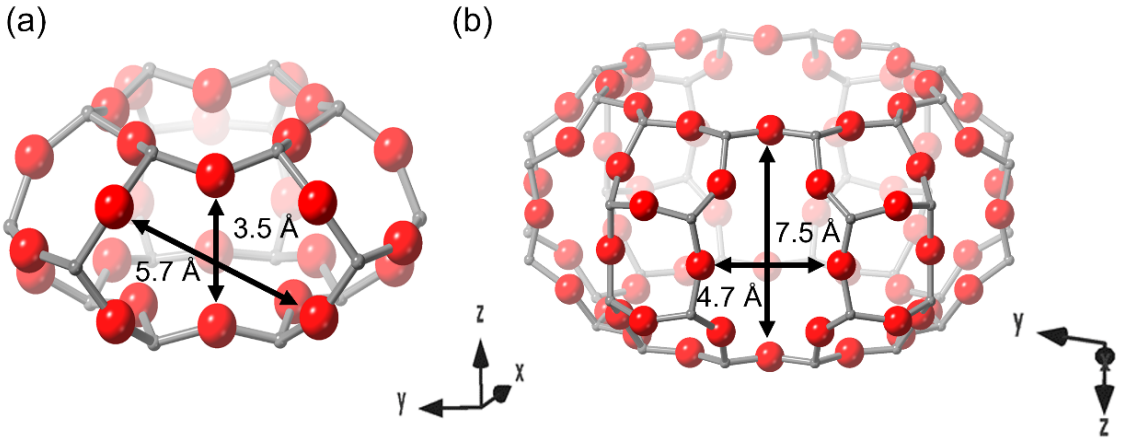

Figure 4. Representation of the framework structure that makes up (a) the *ste* cage and (b) the *can* cage.

After the calcination step, 2.8 K^+ cations are available in the main channel sites for subsequent aqueous ion exchange with La^{3+}, and repeated ion exchange gives $K_{2.7}La_{2.1}$-L. Again, dehydration at 573 K results in migration from site III to site II, but no increase in the La content of site I, whereas calcination at 1073 K results in further migration of La^{3+} to site I. Additional extensive ion exchange with La^{3+} and calcinations result in further site displacements and inter-site rearrangements until all K^+ cations are exchanged with La^{3+} cations in all three sites and $La_{3.0}$-L zeolite is obtained (Tables 1 and 2). In dehydrated zeolite $La_{3.0}$-L the cations occupy mainly sites I and II (Figure 5). Unlike for $K_{9.0}$-L, very few cations (0.26 La^{3+} per unit cell, Table 1) were found at site III.

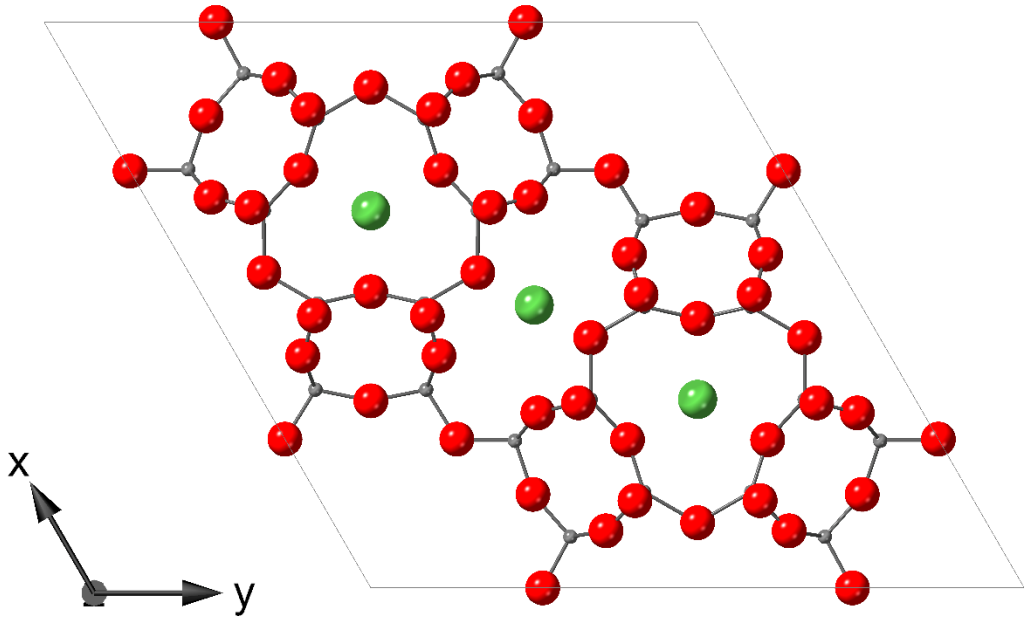

Figure 5. Representation of the dehydrated structure of zeolite $La_{3.0}$-L with cations occupying sites I and II (O red, Si or Al grey, La green).

Replacement of larger K^+ cations with smaller La^{3+} cations in the *can* cage leads to a reduction in the unit cell parameters *a* (18.45 to 18.14 Å) and *c* (7.5 to 7.4 Å) and as a result, the unit cell volume contracts from 2204.66 to 2099.32 $Å^3$. The T-O bond lengths are in all cases within an acceptable range of 1.58 Å to 1.70 Å. Notably the T_1-O_1-T_1 and T_2-O_5-T_2 angles have decreased significantly (by ca. 10% in each case) as a result of distortion of the framework to coordinate to the smaller La^{3+} cations in sites I and II, (Table 1).[24]

Direct evidence of the La^{3+} cations exchanging K^+ cations in the *can* cages was obtained by high-resolution STEM of zeolite $La_{3.0}$-L. Images with atomic resolution were recorded on $K_{9.0}$-L and $La_{3.0}$-L using the Cs-corrected STEM-ADF method described elsewhere and are presented in Figure 6.[25,26] Figures 6 (b) and (e) have been Wiener filtered in order to improve the signal-to-noise ratio. For $La_{3.0}$-L, the [0 0 1] projection shows atomic resolution images of the zeolitic framework with localized regions of high intensity in the *can* cages, which are attributed to the lanthanum atoms, which have much higher electron scattering factors than the

aluminosilicate framework. Images taken over an extended area show that the material is very well ordered, and lanthanum atoms are evenly and atomically dispersed, with no indication of lanthanum clusters. Bright regions are also observed sporadically observed in site II, where the occupancy of La^{3+} is only 0.33. A simulated image, using the crystallographic structure determined by Rietveld refinement, matches the observed filtered image closely. By comparison, an image of $K_{9.0}$-L (although of lower quality) shows regions of similar intensity corresponding to both tetrahedral framework cations and extra-framework cation sites in the *can* cages, as predicted in the simulated image.

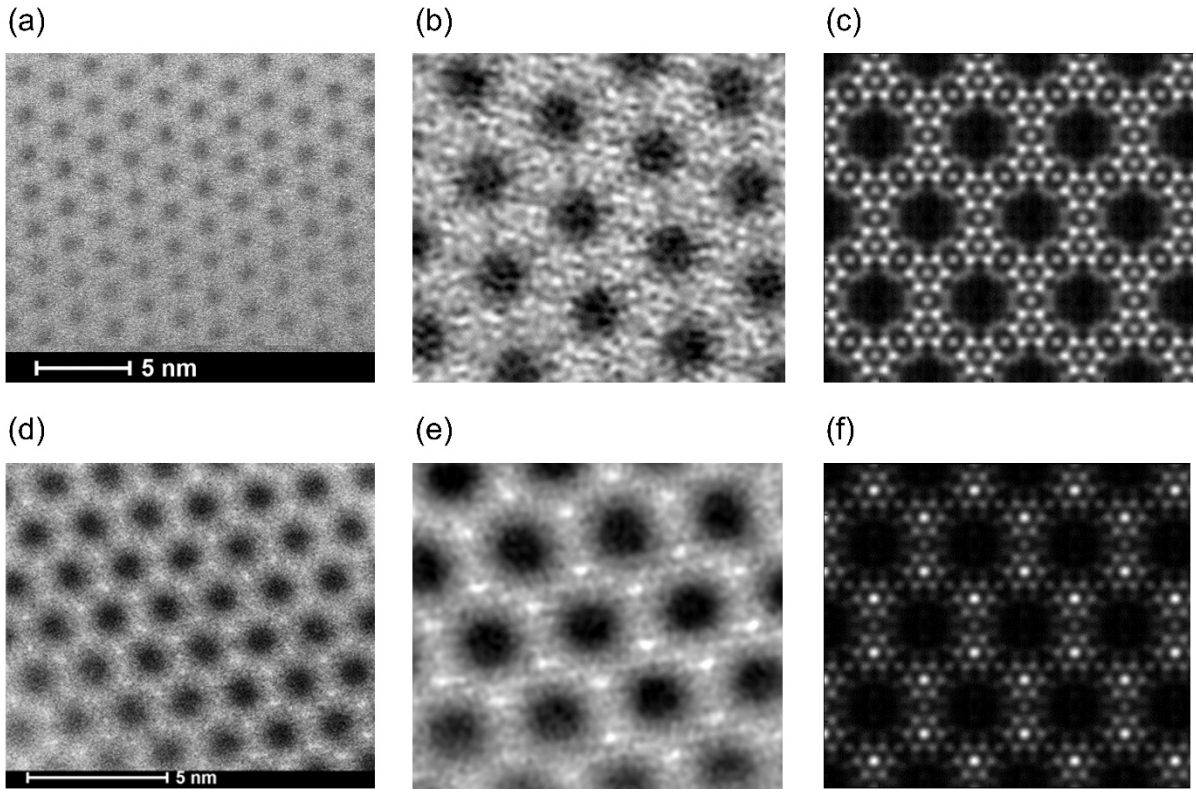

Figure 6. Cs-corrected STEM-ADF images of $K_{9.0}$-L ((a) and (b)) and $La_{3.0}$-L ((d) and (e)) taken along the [001] zone axis. Images (b) and (e) were Wiener filtered to reduce noise. Images (c) and (f) were simulated using the QSTEM software.

Additionally, STEM imaging of La_3-L revealed an isolated feature, shown in Figure 7, where a ring of six bright spots that indicate columns of *can* cages occupied by La^{3+} cations are rotated

by 30° related to the surrounding framework. Previous analysis of high resolution TEM micrographs of K-L identified similar features as rotational defects where a group of six columns of *can* cages and *d6r*s around a large channel are rotated by 30°, while retaining full tetrahedral connectivity.[27] On the basis of this structural model of the rotational defect, the ion exchange properties of the zeolite would not be strongly affected and the observed La^{3+} distribution shown by the STEM image of La_3-L is consistent with this.

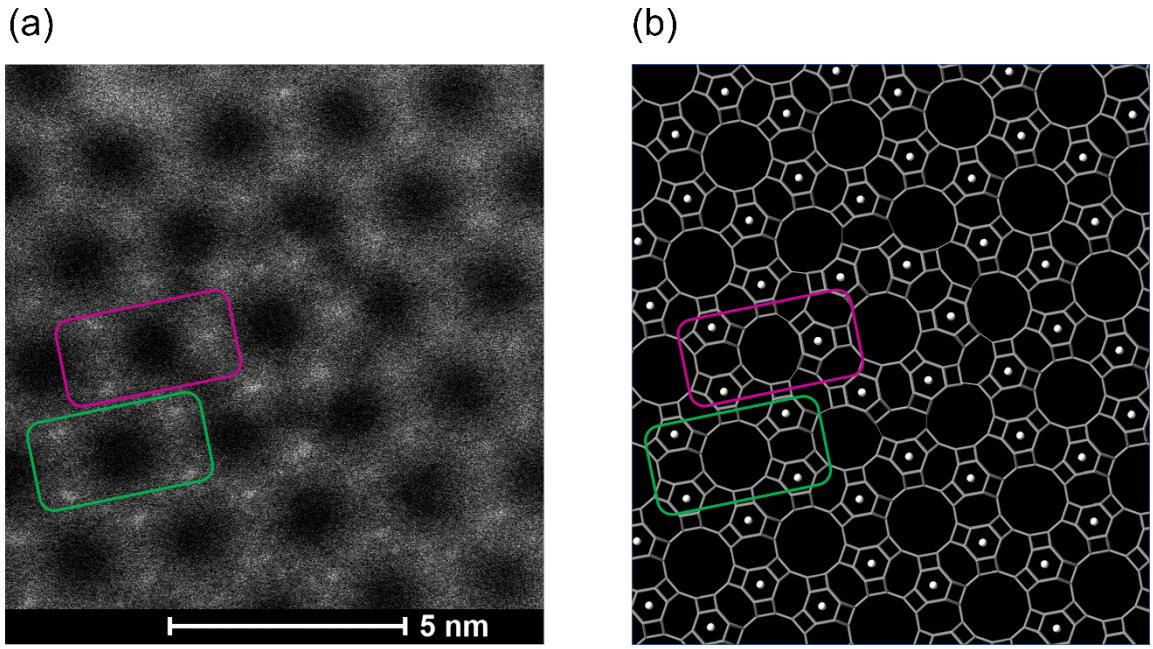

Figure 7. (a) Experimental STEM image of La-LTL down [001] showing a rotational defect described in the text and (b) schematic illustration of the defect with lines indicating T-T linkages and white dots representing La cations in *can* cages. Purple and green boxes illustrate different arrangements of *can* cages close to, and distant from, the defect core. In (b) T-O-T links between the defect and the surrounding framework are represented by faint lines.

Finally, a colour change from white to light pink was observed for samples exchanged with La^{3+} cations and calcined (SI, S7). This may indicate the existence of structural defects caused by the breaking of T-O bonds that are not reformed.

In summary, it is possible to replace all K^+ cations in K-L by La^{3+} via repeated aqueous ion exchange and calcination. The driving force is the tendency for La^{3+} to occupy closed, cage sites. The cations in site I of the L framework are closely coordinated to six O atoms, in site II to four and in site III to two (Table 2). Since extra-framework cations favour sites where they can achieve their maximum coordination, sites I and II are energetically the most favorable for both K^+ and La^{3+} cations in the dehydrated zeolite L. In dehydrated zeolite $K_{9.0}$-L sites I and II are fully occupied (2 K^+ and 3 K^+ cations per unit cell, respectively) whereas the occupancy of site III, which can be exchanged in solution, is *ca*. 67 % (4 K^+ cations per unit cell). To get full exchange, coordinated motion of K^+ and La^{3+} ions from and to sites I and II is required (Table 1).

Access to sites I and II requires adjacent vacant sites to be present, to allow K^+ to leave and be replaced by La^{3+}. It also requires the removal of bound water molecules from the La^{3+} cations. The rate determining step for the inclusion of La^{3+} in site I will be the exit of K^+ cations (ionic radius 1.38 Å,[28]) through non-planar 6-rings (in *can* cages, these have a crystallographic free diameter of ca. 0.8 Å). For the exit of K^+ from the *can* cage this requires a high amount of thermal energy and so a high temperature to occur. As previously observed in other zeolites, phonon modes cause 'breathing' of pore windows which helps the expansion of the narrow 6MR permitting cation movement.[29,30] Hence, the existence of vacancies in sites II and III, and a high calcination temperature which causes removal of water molecules and enhances framework vibrations, enable the K^+ cation diffusion from site I towards site II, then site III followed by the counter migration of La^{3+} cations from site II to site I, resulting in the internal ion exchange. The proposed internal ion exchange mechanism for zeolite L is shown in Figure 8.

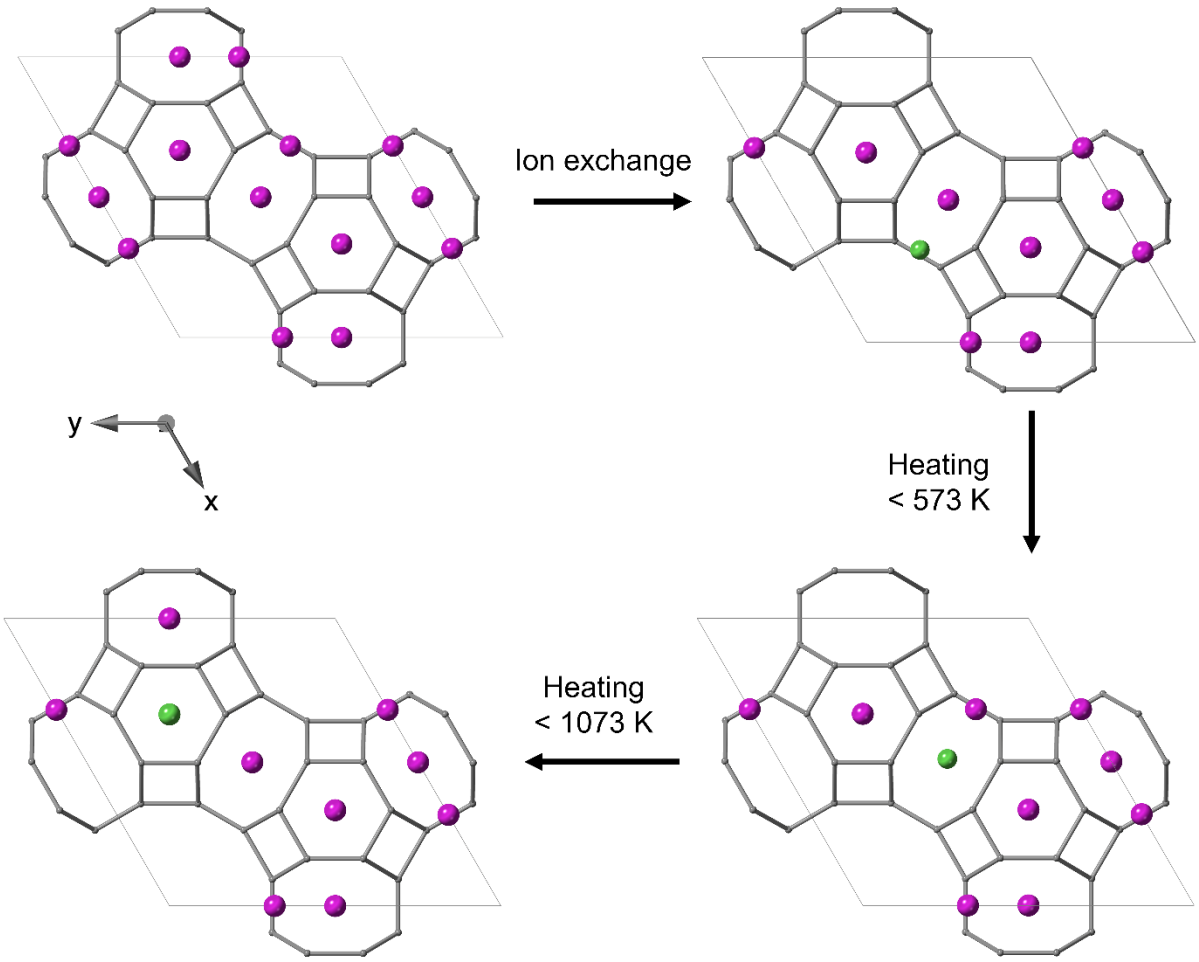

Figure 8. Internal ion exchange mechanism (K pink and La green). Framework O atoms are omitted for clarity and T−T linkages are represented by grey sticks.

According to Rietveld refinement, the number of extra-framework cations in main channel sites per unit cell decreases from 4 to 2.8 to 1.9 to 0.3 in the calcined forms of zeolites $K_{9.0}$-, $K_{5.7}La_{1.1}$-, $K_{2.7}La_{2.1}$- and $La_{3.0}$-L. To investigate the effect of this on adsorption, CO_2 adsorption isotherms at 298 K were measured (Figure 9).

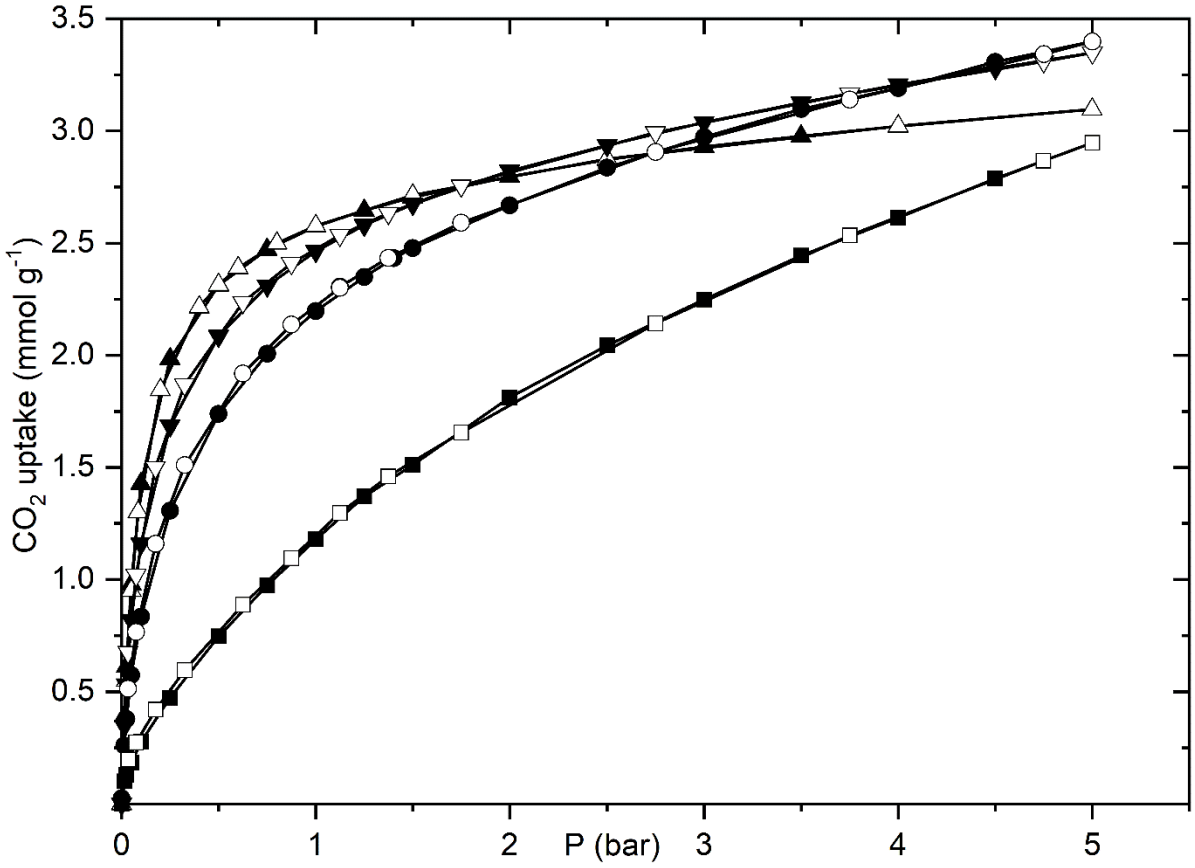

Figure 9. CO_2 isotherms at 298 K on $K_{9.0}$-L (▲), $K_{5.7}La_{1.1}$-L (▼) $K_{2.7}La_{2.1}$-L (●) and $La_{3.0}$-L (■). Adsorption, closed symbols; desorption, open symbols.

All the zeolite L materials showed similar uptakes at 5 bar, of 3-3.5 mmol g^{-1}. However, the steepness of the isotherms decreases as the La-content increases, the decrease being most marked for the $La_{3.0}$-L Henry Law constants (calculating neglecting very small initial uptakes *ca*. 0.1 mmol g^{-1} at pressures close to zero) are given in Table 3 and Supporting Information, S8. They indicate a sharp reduction from 36.6 mol (kg bar)$^{-1}$ in samples containing appreciable numbers of K^+ cations in accessible main channel sites to 1.80 mol (kg bar)$^{-1}$ for $La_{3.0}$-Lwhere there are very few main channel cations.

Table 3. Henry's law constants at 298 K for LTL and FAU samples ($K_0 = \ln(K_H)$). For $La_{3.0}$-L sample, the effect of very small initial uptake (*ca*. 0.1 mmo g^{-1}) is neglected.

Sample	$K_{9.0}$-L	$K_{5.7}La_{1.1}$-L	$K_{2.7}La_{2.1}$-L	$La_{3.0}$-L	$Na_{56.0}$-Y	$La_{18.7}$-Y
K_0	3.60(2)	3.60(3)	3.13(5)	0.59(3)	3.66(1)	0.51(5)
K_H (mol (kg bar)$^{-1}$)	36.60(2)	36.60(3)	22.90(5)	1.80(3)	38.90(1)	1.66(5)

Measurements of isosteric heats of adsorption on $K_{9.0}$-L and $La_{3.0}$-L were also made from the CO_2 isotherms at 278, 288 and 298 K, as shown in Figure 10, using the Clausius-Clapeyron equation (Supporting Information, S9). Table 4 documents a strong decrease in the heat of adsorption (measured over the range of 0.75 to 1.5 mmol g^{-1}) from ca. 35 kJ mol^{-1} in $K_{9.0}$-L to 28 - 20 kJ mol^{-1} in $La_{3.0}$-L. The higher value is similar to those observed previously for Na-Y,[31–33] for example, whereas the lower value is closer to those values (ca. 20 kJ mol^{-1}) observed for high silica large pore materials such as dealuminated Y,[32] pure silica Beta[34,35] and high silica MCM-41,[36] where few or no extra-framework cations are present. Notably, although TGA indicates that $La_{3.0}$-L shows the lowest water loss of all of the L zeolites measured (Figure S6), it is not hydrophobic.

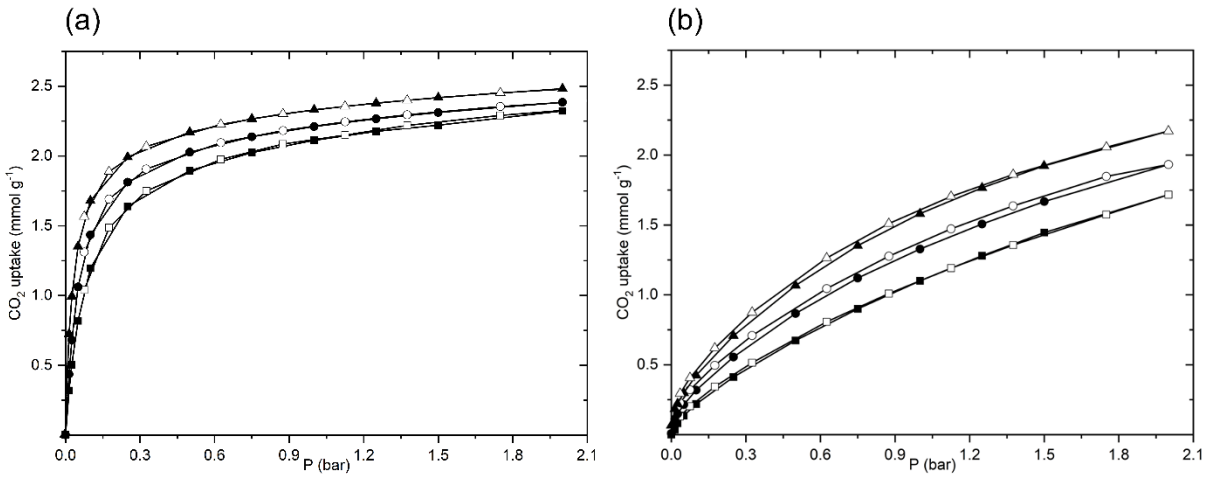

Figure 10. CO_2 isotherms at 278 K (▲), 288 K (●) and 298 K (■) on (a) $K_{9.0}$-L and (b) $La_{3.0}$-L. Adsorption, closed symbols; desorption, open symbols.

Table 4. Isosteric heats of adsorption (ΔH) measured over the range 0.75 - 1.5 mmol g^{-1} for $K_{9.0}$-L and $La_{3.0}$-L.

Sample	ΔH (kJ mol^{-1}) at 0.75 mmol g^{-1}	ΔH (kJ mol^{-1}) at 1.0 mmol g^{-1}	ΔH (kJ mol^{-1}) at 1.25 mmol g^{-1}	ΔH (kJ mol^{-1}) at 1.5 mmol g^{-1}
$K_{9.0}$-L	36(3)	34.8(7)	34.8(2)	35.3(2)
$La_{3.0}$-L	28(3)	25.6(7)	21.9(2)	20.1(5)

One potential advantage of zeolites with shallow CO_2 isotherms as sorbents is that the working capacity in pressure swing adsorption (PSA) between high pressure and (say) 1 bar will be increased. To see if the effect of La^{3+} in L could be replicated by a cheaper cation (Ca^{2+}), as-prepared zeolite $K_{9.0}$-L was exchanged with Ca^{2+} cations via aqueous and internal ion exchanges. Two mixed-cation zeolites were prepared with the compositions $K_{6.2}Ca_{1.4}$-L and $Ca_{3.8}K_{1.4}$-L but efforts to completely exchange K^+ cations with Ca^{2+} cations were unsuccessful. The resulting PXRD patterns showed a zeolite with composition $Ca_{4.0}K_{1.2}$-L with an increased background and additional peaks that indicate that part of the structure has decomposed (SI, S10). Due to the very similar X-ray scattering coefficients for calcium and potassium, it was impossible to determine which cations occupy sites by using PXRD data for Rietveld refinement. Rather, it was inferred that Ca^{2+} cations are exchanging K^+ cations in sites I and II (i) from the lower number of cations present in site III (one per unit cell for $Ca_{3.8}K_{1.4}$-L) and (ii) the contraction of the *a* and *c* (18.45 to 18.22 Å and 7.5 to 7.3 Å), consistent with replacement of K^+ with a smaller cation, by analogy with La-L (SI, S11). The CO_2 adsorption isotherms show a similar trend to that observed for the La-exchanged series, but due to the presence of cations in the 12MR channel in all samples the interaction with CO_2 is stronger and the working capacity for PSA at moderate CO_2 desorption pressures is reduced (SI, S12).

For comparison with La-L, a fully La-exchanged zeolite Y (Si/Al = 2.4) was also prepared. The literature[6] indicates that La^{3+} cations favour sites in the sodalite (*sod*) cages in zeolite Y, which, like sites I and II in zeolite L, are inaccessible to adsorbed molecules larger than H_2O,

such as CO_2. Aqueous ion exchange of Na-Y only results in exchange of Na^+ cations from the supercages by La^{3+}, but subsequent heating at 673 K enables internal ion exchange by which La^{3+} cations replace Na^+ cations in the *sod* cage. Again, the driving force is for the La^{3+} cations to achieve more energetically favourable positions when dehydrated. A lower temperature is required for the process in Y than for L because no vacant sites have to be generated to allow initial exit of cations from the closed sites and the rate determining step involves a smaller cation migrating through a larger window (the 6R of *sod* is planar, where the 6R of *can* is puckered). Repeated aqueous and internal cation exchange at 673 K gave La-Y with unit cell composition $La_{18.7}Al_{56.0}Si_{136.0}O_{384}$ ($La_{18.7}$-Y). Rietveld analysis confirmed that while 30.4 Na^+ cations per unit cell are in supercage sites in Na-Y, and therefore accessible to CO_2, in La-Y all 18.7 La^{3+} cations are located in inaccessible *sod* cages (Figure 11, also SI, S4 and S13).

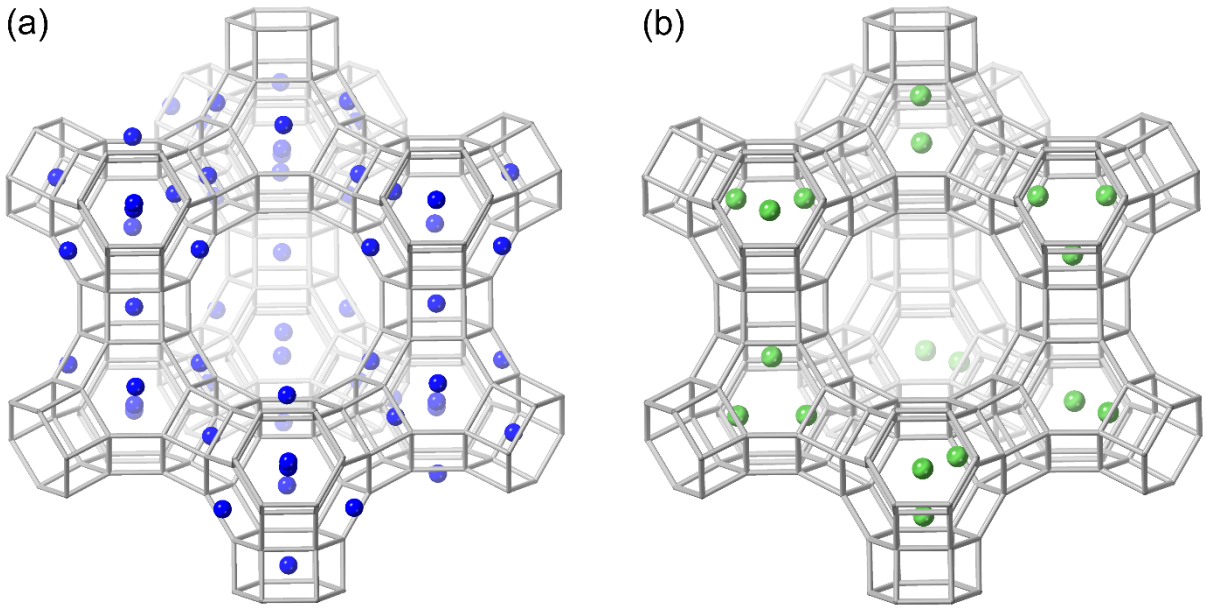

Figure 11. Structural representation of cation positions in zeolite (a) Na_{56}-Y and (b) $La_{18.7}$-Y, showing Na^+ cations occupying sites in the large cages in Na-Y while these cages are empty in La-Y.

The effect on the CO_2 isotherms is marked (Figure 12) and similar to that observed for zeolite L. The La-Y isotherm is much less steep than that on Na-Y and, neglecting an initial uptake of ca. 0.2 mmol g^{-1}, gives a much lower Henry Law constant than measured for the Na-Y (1.66 mol (kg bar)$^{-1}$ compared to 38.9 mol (kg bar)$^{-1}$, Table 3 and SI, S8), indicating a much weaker interaction with CO_2. While the shapes of the isotherms of La-Y and La-L are similar, the specific uptake on La-Y is greater (2.77 mmol g^{-1} vs. 1.81 mmol g^{-1} at 2 bar, 298 K), because of the greater total pore volume of zeolite Y.

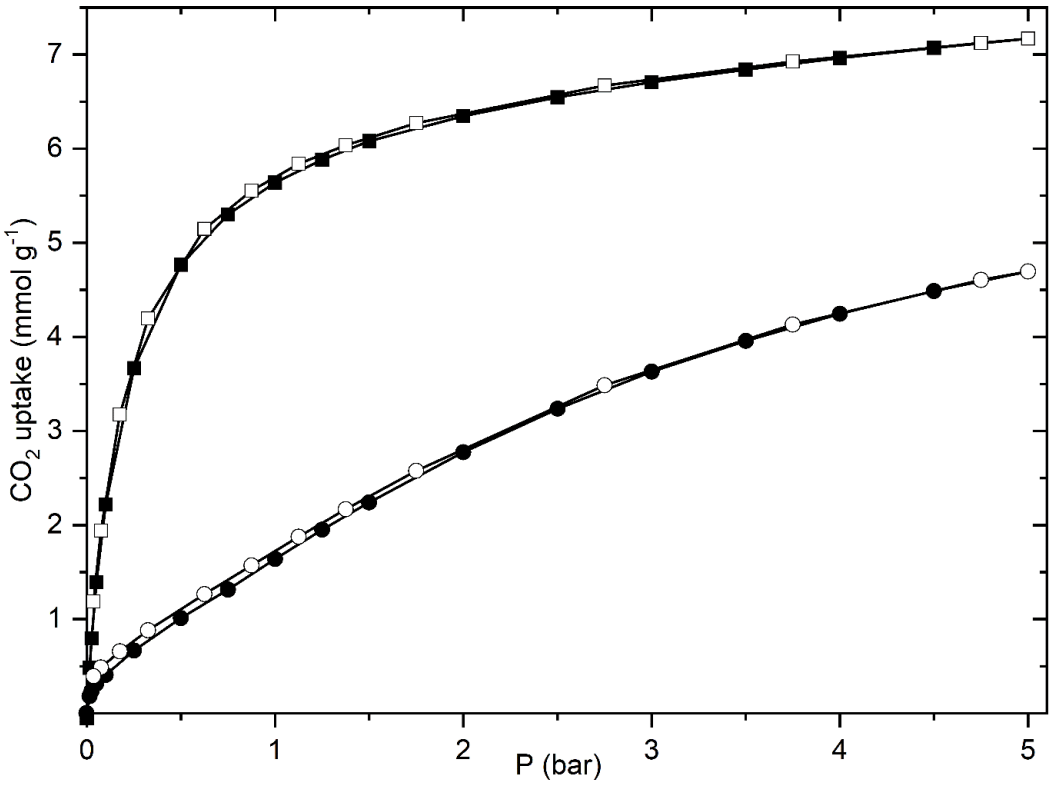

Figure 12. CO_2 isotherms at 298 K on Na-Y (■) and La-Y (●). Adsorption, closed symbols; desorption, open symbols.

These studies give insight on the mechanism of internal cation exchange in zeolites with low Si/Al ratios. They also indicate that 'hiding' polyvalent cations in small zeolite cages produces porous materials (without Brønsted acidity, and therefore with enhanced stability) that have highly charged frameworks but no accessible cations. These are unusual environments for

adsorption, and their CO_2 isotherms have lower slopes and Henry Law constants than typical alkali metal zeolites. As a result, they would have enhanced working capacities for CO_2 pressure swing adsorption with 1 bar or less as the lower desorption pressure, where very high (and expensive) vacuum or temperature swing processes would not be necessary. The prolonged procedure required to prepare La-L reported here, including repeated high temperature calcination, would prevent its practical implementation, but La-Y is easier to prepare, has similar properties, and higher specific uptakes, and therefore offers a more feasible option.

Conclusions

These investigations shed light on the mechanism of internal cation exchange in zeolite L (and Y) and also demonstrate the adsorption properties of unusual zeolite compositions with highly charged frameworks but very few accessible extra-framework cations.

A series of K,La-L samples in which K has been progressively replaced by La has been prepared and the location of the La^{3+} cations estimated by Rietveld refinement. This required a combination of aqueous ion exchange of main channel K^+ cations with La^{3+} followed by heating that facilitates the migration of La^{3+} first into site II (possible at 573 K) and then into site I (possible at 1073 K). In each case this ejects K^+ into main channel sites, so exhaustive cycling eventually enables complete exchange. The structure of fully exchanged $La_{3.0}$-L was measured by Rietveld analysis, showing only closed sites in *can* and *ste* cages are occupied. It was also imaged by STEM, and the La^{3+} cations were readily observed in sites I and II. By contrast, complete ion exchange of zeolite $K_{9.0}$-L with Ca^{2+} cations was not possible and only a partial exchange was achieved, up to a Ca^{2+} cation content of ca. 84 %.

A mechanism for the internal ion exchange process of K^+ by La^{3+} has been proposed. La^{3+} cations enter the *ste* and *can* cages through 8Rs or 6Rs, respectively, after K^+ cations exit to a vacant site through the same windows. For the latter process to occur a very high temperature treatment is necessary. The migration of La^{3+} cations toward the *can* cage is thermodynamically driven by the loss of bound water molecules and the more favourable site I coordination, while it is kinetically permitted by enhanced structural vibrations at high temperature.

Additionally, the effect of reducing the number of cations in the 12R channel on the shape of the CO_2 isotherm at 298 K was investigated. 'Hiding' a majority of cations in sites I and II from adsorbed molecules entering the large channels resulted in weaker interactions, isotherms with lower slopes and lower Henry Law constants. Such isotherms are of interest for enhanced working capacities in pressure swing adsorption with relatively high desorption pressures, but the preparation route used is too protracted to be of commercial interest. By contrast, zeolite La-Y, in which the La^{3+} cations are also in cages and inaccessible to CO_2 molecules, was found to show a similar adsorption isotherm shape to La-L, with higher capacity, and can be prepared more readily, using lower internal ion exchange temperatures, and is a target for more detailed studies of adsorption and separation.

Conflicts of interest

There are no conflicts to declare

Acknowledgements

The authors gratefully acknowledge the EPSRC (FLEXICCS – Flexible Industrial Carbon Capture, EPSRC EP/N024613/1 (MML, SB and PAW) and Capital for Great Technologies, EP/L017008/1 (DNM)) for funding, Maria Nowosielska for assistance with recording the

adsorption isotherms, Andrew Boyes and Lewis Clough for their contribution in collecting the data, and Johnson Matthey for providing the zeolite Na-Y sample.

The research data underpinning this publication can be accessed at https://doi.org/10.17630/1fff8eca-c51d-4c6e-a8a9-0ec83939479c [37]

References

1 E. G. Derouane and D. J. Vanderveken, *Appl. Catal.*, 1988, **45**, 15–22.

2 G. Larsen and G. L. Haller, *Catal. Letters*, 1989, **3**, 103–110.

3 P. Li, Y. Wang, H. Li and G. Calzaferri, *Angew. Chemie Int. Ed.*, 2014, **53**, 2904–2909.

4 Y. Wang, H. Li, L. Gu, Q. Gan, Y. Li and G. Calzaferri, *Microporous Mesoporous Mater.*, 2009, **121**, 1–6.

5 P. A. Newell and L. V. C. Rees, *Zeolites*, 1983, **3**, 22–27.

6 D. H. Olson, G. T. Kokotailo and J. F. Charnell, *J. Colloid Interface Sci.*, 1968, **28**, 305–314.

7 G. T. Kokotailo and S. L. Lawton, US Patent, 3,640,680, 1968.

8 P. Ballirano and G. Cametti, *Microporous Mesoporous Mater.*, 2012, **163**, 160–168.

9 P. Ballirano, A. Pacella, A. Bloise, M. Giordani and M. Mattioli, *Minerals*, 2018, **8**, 28–44.

10 J. L. Schlenker, J. J. Pluth and J. V. Smith, *Acta Crystallogr. Sect. B Struct. Crystallogr. Cryst. Chem.*, 1977, **33**, 3265–3268.

11 P. Ballirano, A. Bloise, C. Cremisini, M. Elisa Nardi, R. Montereali and A. Pacella, *Period. di Mineral.*, 2018, **87**, 123–134.

12 H. S. Sherry, *Clays Clay Miner.*, 1979, **27**, 231–237.

13 J. Mon, Y. Deng, M. Flury and J. B. Harsh, *Microporous Mesoporous Mater.*, 2005, **86**, 277–286.

14 D. Keir, E. F. T. Lee and L. V. C. Rees, *Zeolites*, 1988, **8**, 228–231.

15 X. Shu, W.Fu, M. He, M. Zhou, Z. Shi and S. Zhang, European Patent, 0,550,917 A1, 1992.

16 J.P. Verduijn, US Patent, 5,242,675, 1992.

17 C. T. Koch, Determination of Core Structure Periodicity and Point Defect Density Along Dislocations, Ph.D. thesis, ASU, Arizona, 2002.

18 Eli Luberoff, Desmos, www.desmos.com, 2011.

19 B. H. Toby, *J. Appl. Crystallogr.*, 2001, **34**, 210–213.

20 P. A. Wright, J. M. Thomas, A. K. Cheetham and A. K. Nowak, *Nature*, 1985, **318**, 611–614.

21 L. Gigli, R. Arletti, S. Quartieri, F. Di Renzo and G. Vezzalini, *Microporous Mesoporous Mater.*, 2013, **177**, 8–16.

22 X. Du, H. Zhang, X. Li, Z. Tan, H. Liu and X. Gao, *Chinese J. Catal.*, 2013, **34**, 1599–1607.

23 R. M. Barrer and H. Villiger, *Zeitschrift für Krist.*, 1969, **128**, 352–370.

24 J. V. Smith, *Chem. Rev.*, 1988, **88**, 149–182.

25 A. Mayoral, T. Carey, P. A. Anderson and I. Diaz, *Microporous Mesoporous Mater.*, 2013, **166**, 117–122.

26 A. Mayoral, P. A. Anderson and I. Diaz, *Micron*, 2015, **68**, 146–151.

27 T. Ohsuna, B. Slater, F. Gao, J. Yu, Y. Sakamoto, G. Zhu, O. Terasaki, D. E. W.

Vaughan, S. Qiu and C. R. A. Catlow, *Chem. - A Eur. J.*, 2004, **10**, 5031–5040.

28 R. D. Shannon, *Acta Crystallogr. Sect. A*, 1976, **32**, 751–767.

29 K. D. Hammonds, H. Volker and M. T. Dove, *J. Phys. Chem. B*, 1998, **102**, 1759–1767.

30 K. D. Hammonds, H. Deng, V. Heine and M. T. Dove, *Phys. Rev. Lett.*, 1997, **78**, 3701–3704.

31 H. V. Thang, L. Grajciar, P. Nachtigall, O. Bludský, C. O. Areán, E. Frýdová and R. Bulánek, *Catal. Today*, 2014, **227**, 50–56.

32 G. Maurin, P. L. Llewellyn and R. G. Bell, *J. Phys. Chem. B*, 2005, **109**, 16084–16091.

33 S. Cavenati, C. A. Grande and A. E. Rodrigues, *J. Chem. Eng. Data*, 2004, **49**, 1095–1101.

34 T. D. Pham, R. Xiong, S. I. Sandler and R. F. Lobo, *Microporous Mesoporous Mater.*, 2014, **185**, 157–166.

35 L. Grajciar, J. Čejka, A. Zukal, C. Otero Areán, G. Turnes Palomino and P. Nachtigall, *ChemSusChem*, 2012, **5**, 2011–2022.

36 Y. Belmabkhout, R. Serna-Guerrero and A. Sayari, *Chem. Eng. Sci.*, 2009, **64**, 3721–3728.

37 M. M. Lozinska, D. N.Miller, S. Brandani, P. A. Wright, 2019, Dataset. University of St Andrews Research Portal. https://doi.org/10.17630/1fff8eca-c51d-4c6e-a8a9-0ec83939479c